

Magmatic–hydrothermal origin of Nevada's Carlin-type gold deposits

John L. Muntean^{1*}, Jean S. Cline², Adam C. Simon² and Anthony A. Longo²

The Eocene epoch in the Great Basin of western North America was a period of profuse magmatism and hydrothermal activity. During that period, the Carlin-type gold deposits in Nevada were produced, Earth's second largest concentration of gold after deposits in South Africa. The characteristics of the Carlin-type deposits have been documented, but a widely acceptable explanation for their genesis is outstanding. Here we integrate microanalyses of ore minerals, experimental data that describe metal partitioning, and published age and isotopic data, to suggest that the gold is sourced from magma. We relate gold deposition to a change from shallow subduction to renewed magmatism and the onset of extension. We propose that upwelling asthenosphere impinged on a strongly modified subcontinental lithospheric mantle, generating magmas that released gold-bearing fluids at depths of 10 to 12 km. The rising aqueous fluids with elevated hydrogen sulphide concentrations and a high ratio of gold to copper underwent phase changes and mixed with meteoric water. Within a few kilometres of the surface, the fluids dissolved and sulphidized carbonate wall rocks, leading to deposition of gold-bearing pyrite. We conclude that the large number and size of Carlin-type deposits in Nevada is the result of an unusual convergence of a specific geologic setting, together with a tectonic trigger that led to extremely efficient transport and deposition of gold.

The Eocene epoch in the Great Basin of western North America was a period of intense hydrothermal activity brought on by a shift from shallow subduction and compressional tectonics to renewed magmatism coincident with extensional tectonics. The most important economic manifestation of this activity is the formation of Carlin-type gold deposits (CTGDs) in northern Nevada, which contain over 6,000 tons of gold (Au), constituting the second largest concentration of Au in the world¹ (Fig. 1). The deposits account for ~6% of annual worldwide production, making the United States the fourth largest producer of Au. CTGDs are hydrothermal replacement bodies hosted primarily by lower Palaeozoic miogeoclinal carbonate rocks, in which Au occurs in solid solution or as submicrometre particles in pyrite. Salient features of the four largest clusters of deposits (Carlin trend, Cortez, Getchell, Jerritt Canyon; Fig. 1), which account for >90% of the Au in CTGDs worldwide, are listed in Table 1. These characteristics indicate that common processes led to the formation and transportation of Au-bearing hydrothermal fluids and deposition of Au; however, these ubiquitous features have not been sufficiently diagnostic to yield a widely accepted genetic model. Two endmember models that describe the proposed origin of Au in CTGDs include: (1) magmatic–hydrothermal models, in which Au was derived from magmas; and (2) amagmatic models, wherein Au was sourced from the crust by meteoric or metamorphic waters¹.

Here, we propose a model for the origin of CTGDs that (1) describes the formation of a primitive ore fluid and tracks that fluid through Au deposition, and (2) relates the fluid and CTGDs to subduction processes and deep crustal magma evolution brought about by a change in tectonics. This model evolved in response to new data we generated and recently published data that demonstrate a closer temporal and spatial link between deposit formation and magmatism than was previously reported. These data include geochronologic data, which demonstrate that formation of the CTGDs tracked the southwestern sweep of Eocene

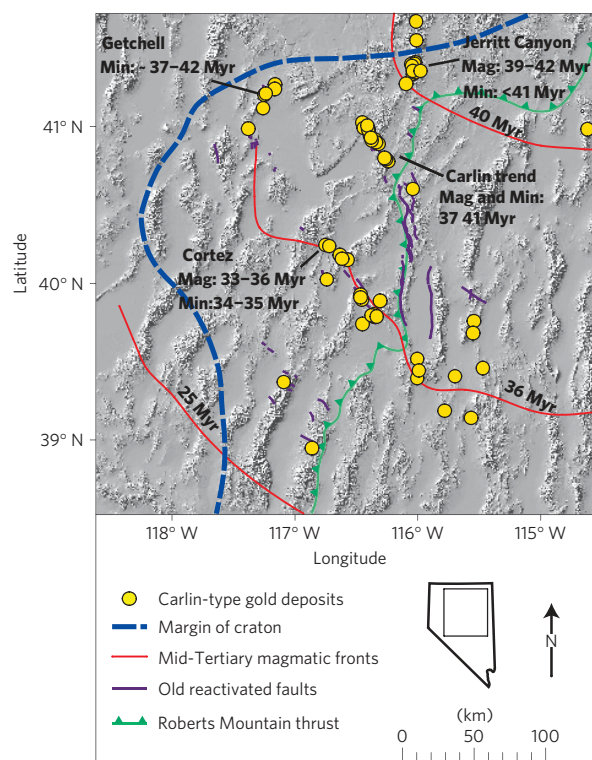


Figure 1 | Locations of CTGDs in northern Nevada. Locations of the four main clusters of CTGDs and their estimated age of mineralization (Min) and associated magmatism (Mag). Also shown are the margin of the underlying Precambrian craton (based on Sr isotopes), Mid-Tertiary magmatic fronts (limits of advance towards southern Nevada at indicated times), locations of old reactivated fault systems, and the easternmost extent of the Roberts Mountain thrust fault.

¹Nevada Bureau of Mines and Geology, Mail Stop 178, University of Nevada Reno, Reno, Nevada, 89557-0178, USA, ²University of Nevada, Las Vegas, Department of Geoscience, 4505 Maryland Parkway, PO Box 454010, Las Vegas, Nevada, 89154-4010, USA. *e-mail: munteanj@unr.edu.

Table 1 | Characteristics of CTGDs in Nevada.

- | | |
|---|---|
| 1 | Formed from 42 to 34 Myr BP, corresponding to a change from compression to extension and renewed magmatism in northern Nevada. |
| 2 | Occur in clusters along old, reactivated basement rift structures, preferentially hosted by carbonate-bearing rocks within or adjacent to structures in the lower plate of a regional thrust. |
| 3 | Similar hydrothermal alteration and ore paragenesis: dissolution and silicification of carbonate, sulphidation of Fe in the rock, formation of Au-bearing arsenian pyrite, and late open-space deposition of orpiment, realgar and stibnite. Ore signature is Au-Tl-As-Hg-Sb-(Te), with low Ag and base metals. |
| 4 | Non-boiling ore fluids ranged from ~180 to 240 °C and were of low salinity (mostly ≤ 6 wt% NaCl eq.) and CO ₂ -bearing (<4 mol %); illite and local kaolinite indicate acidic fluids. |
| 5 | Formation depth <3 km. Lack of mineral or elemental zoning at the scale of <5–10 km laterally and <2 km vertically suggests minor temperature gradients. No known coeval porphyry copper, skarn or distal Ag-Pb-Zn mineralization in the clusters of CTGDs. |

magmatism in time and space across Nevada^{1–4} (Fig. 1). Further support for a magmatic connection is provided by H and O isotope data collected from fluid inclusion waters and ore-stage quartz from the Getchell deposit⁵ and from ore-stage kaolinite from some CTGDs (refs 1,2), which are consistent with mixtures of magmatic fluids and meteoric waters. Most other H and O isotope data suggest meteoric water as the source; however, we interpret these data as being consistent with titration of Au-bearing magmatic fluid into meteoric water (see Supplementary Data S1). Sulphur isotope data on ore-stage pyrite range from -4‰ to $+13\text{‰}$ $\delta^{34}\text{S}$ and are consistent with either a sedimentary or magmatic source¹ (see Supplementary Note S1). New laser ablation inductively coupled plasma mass spectrometry (LA-ICP-MS) analyses and electron probe microanalyses (see Supplementary Data S2) demonstrate that ore-stage pyrite contains Au along with As, Hg, Tl, Te, Cu and Sb, an elemental suite that is consistent with transport by magmatic aqueous vapour^{6–9} (see Supplementary Note S2).

Development of optimal geologic setting

An essential first step in the origin of CTGDs was the formation of basement-penetrating rift structures that controlled development of favourable upper crustal structures and stratigraphy. Primarily northwest- and north-striking faults that formed during Mesoproterozoic construction of Rodinia and Neoproterozoic rifting of western North America^{10,11} were critical in controlling subsequent patterns of sedimentation, deformation, magmatism and hydrothermal fluid flow^{12,13}. Following active rifting, a predominantly carbonaceous, carbonate shelf-slope sequence formed along the margin. Reactivation of the underlying basement faults formed second-order basins with variable sedimentary facies, including carbonate debris flow breccias that are important hosts to CTGDs (refs 1,12,13). The Late Devonian to Early Mississippian Antler orogeny, the first in a series of compressional events, thrust deepwater siliciclastic and basaltic rocks eastward over the carbonate shelf-slope, forming the Roberts Mountain thrust fault. The compressional events reactivated underlying basement rift structures, forming fault propagation folds and other features consistent with structural inversion¹³. An optimal setting for the formation of CTGDs was established: structural culminations of highly fractured, reactive carbonate rocks were located above high-angle fault zones linked to underlying basement rift structures and capped by less reactive siliciclastic rocks (Fig. 2).

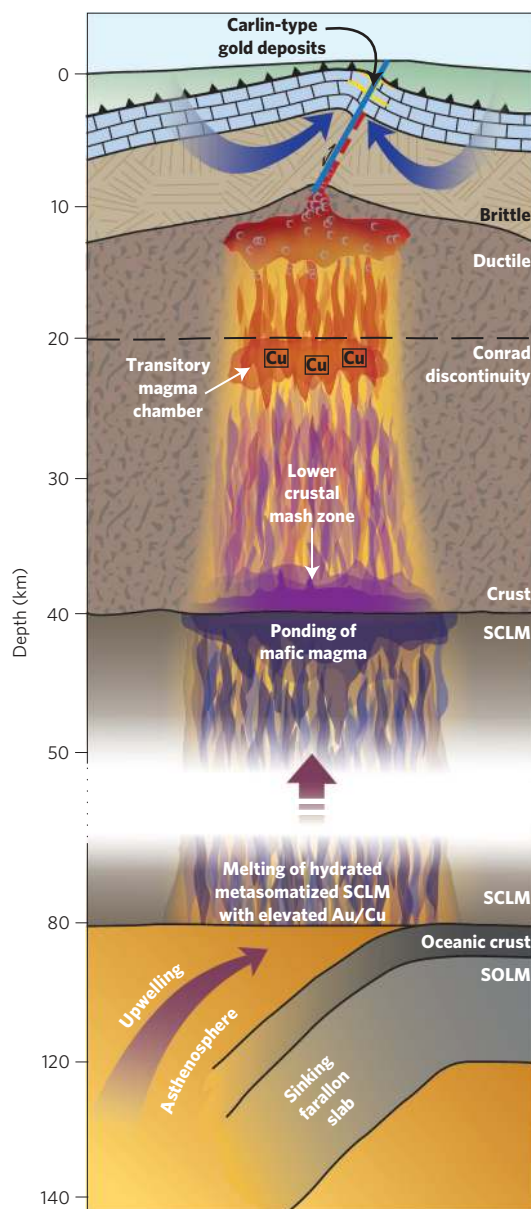


Figure 2 | Schematic cross-section from mantle to the surface (looking east). The points of the model discussed in the text are illustrated. SOLM signifies sub-oceanic lithospheric mantle.

Development of high Au/Cu magmas

A long-lived east-dipping subduction zone was established along western North America by the Middle Triassic period. Back-arc magmatism in Nevada began in the Middle to Late Jurassic period and ended by 65 Myr BP owing to flattening of the subducting Farallon slab¹⁴. During ~175 Myr of arc magmatism and slab dehydration, the mantle wedge beneath the Great Basin was continually hydrated¹⁵ and metasomatized with metals including As, Sb, Tl, Pb, Cu (refs 16–18) and possibly Au (see Supplementary Note S3). Early moderately oxidized magmas may have fractionated a Au-rich sulphide residue during evolution of the subcontinental lithospheric mantle¹⁹ (SCLM; see Supplementary Note S4). During the ~20 Myr of shallow subduction, from ~65 to 45 Myr BP, the base of the SCLM was further hydrated and metasomatized by slab-derived fluids²⁰.

Rollback or delamination of the shallow-dipping slab renewed magmatism at ~45 Myr BP (ref. 21), which swept southwestward at a high angle to the continental margin (Fig. 1). The base of

the fertile, hydrated, metasomatized SCLM with elevated Au/Cu (ref. 19) was exposed to upwelling asthenosphere, resulting in the formation of voluminous, CO_2 -, Cl-, S- and Au-bearing, hydrous, high-alumina basaltic magmas, at an oxygen fugacity f_{O_2} of $\sim \text{FMQ} + 1$ (ref. 22; Fig. 2), where FMQ represents the fayalite–magnetite–quartz buffer. The basaltic magmas underplated and partially melted the overlying continental crust, forming hydrous, S- and Au-bearing, high-K, calc-alkaline magmas of intermediate composition²³ (Fig. 2). The magmas ascended and may have formed transitory magma chambers at the Conrad discontinuity (~ 20 km depth)²⁴, where we propose fractionation of monosulphide solid solution would have preferentially incorporated Cu over Au and further increased the Au/Cu ratio of the ascending melt (Fig. 2). Monosulphide solid solution (mss) is the only sulphide phase to crystallize owing to the low Cu concentration in the melt, which precluded formation of a Cu–Fe–S phase. New experimental data at an f_{O_2} of $\sim \text{FMQ} + 1$, $D_{\text{Cu}}^{\text{mss/melt}} \sim 3,600$ and $D_{\text{Au}}^{\text{mss/melt}} \sim 490$ (see Supplementary Data S3), confirm that monosulphide solid solution preferentially sequesters Cu relative to Au (see Supplementary Note S5).

Generation of ore fluid

As the magmas continued their ascent, they would have reached volatile saturation and released a single-phase (supercritical) CO_2 -, H_2S - (at a high $\text{H}_2\text{S}/\text{SO}_2$ ratio; see Supplementary Note S6) and Au-bearing aqueous fluid with high Au/Cu (Fig. 2). A felsic magma containing 6 wt% H_2O and 1,000 ppm CO_2 would have released an aqueous phase at 400 MPa (~ 15 – 16 km, lithostatic pressure; see Supplementary Note S7). The salinity of this primitive ore fluid was probably between ~ 2 and 12 wt% NaCl eq., on the basis of analyses of fluid and melt inclusions from the deep parts of porphyry Cu deposits and Cl/OH ratios in amphiboles^{16,25}. Experimental data demonstrate that Au and other metals strongly partition from the silicate melt to the volatile phase. For example, analyses of synthetic fluid inclusions trapped in felsic melt–volatile phase assemblages yield vapour/melt partition coefficients for Au ($D_{\text{Au}}^{\text{vapour/melt}}$) at 800°C that range from 12 at 120 MPa with a 2 wt% NaCl eq. vapour, to 56 at 140 MPa with a 9 wt% NaCl eq. vapour^{7,9}. Experimentally determined vapour/melt partition coefficients for Cu ($D_{\text{Cu}}^{\text{aqueous fluid/melt}}$), at similar conditions, are about 300 (ref. 8; see Supplementary Note S8).

Age–composition relationships of dykes and aeromagnetic data along the Carlin trend have identified six distinct Eocene igneous suites that are underlain by individual plutons emplaced at estimated depths of 3–10 km (ref. 3). The plutons comprise a large composite batholith ($\sim 10 \times 40$ km) that was assembled over 4 Myr. The ~ 36 -Myr-old Harrison Pass pluton in the Ruby Mountains, located east of the Carlin trend, further supports the existence of deep Eocene batholithic intrusions. Hornblende geobarometry on this 14-km-diameter, composite granitic pluton suggests magma may have accumulated at a depth of ~ 20 km, before the pluton was emplaced at ~ 12 km, where a rheologic and density contrast between plutonic and metamorphic rocks and overlying sedimentary rocks was present²⁶. Additional evidence for large Eocene magma bodies includes the 39.7-Myr-old Tuscarora caldera (16 km diameter), and the 33.9-Myr-old Caetano caldera that formed by eruption from a magma chamber that measured 20 km by 15 km at a depth of ~ 8 – 10 km (ref. 4). Both calderas formed within a million years of nearby CTGDs in the Carlin trend and Cortez district, respectively. From these data, we conclude that large volumes of Eocene magma stalled at depths of about 10 km near the brittle–ductile transition, forming batholithic-sized felsic intrusions owing to crystallization promoted by devolatilization, and density contrasts with less dense supracrustal rocks.

We conclude that single-phase, H_2S -rich aqueous fluids with high Au/Cu were tapped from reservoirs in the roof zones of plutons

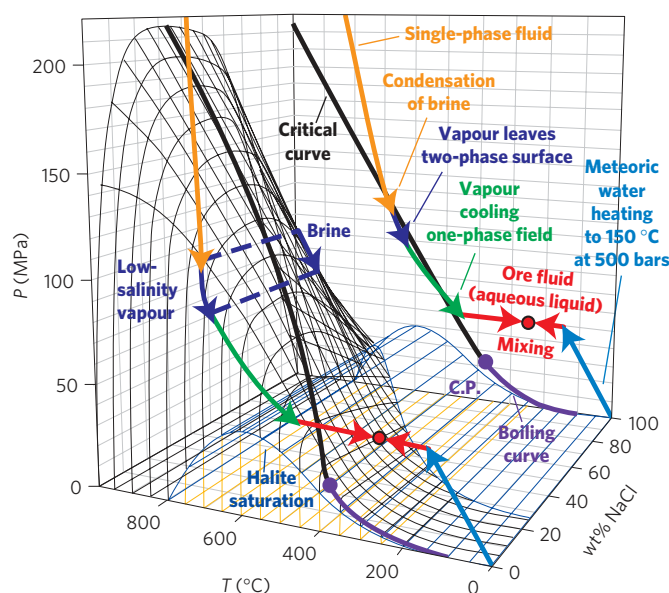


Figure 3 | Phase diagram of the NaCl– H_2O system. The two-phase liquid + vapour surface gridded by isopleths and isotherms is emphasized^{30,32}. The critical curve (heavy black line at crest of two-phase surface) swings across from high salinities at high pressure and temperature (P , T) to lower salinities at lower P and T . The diagram shows fluid paths and important phase changes discussed in the text. The backface shows the projection of the critical curve and fluid paths onto the P – T plane. C.P. signifies the critical point of water.

during extensional reactivation of the high-angle faults linked to underlying basement rift structures (Fig. 2). Low-magnitude extension by pervasive rotational faulting locally occurred in northern Nevada between 36 and 40 Myr BP (refs 1,27). Periodic release of fluid and magma during faulting is supported by leucocratic cupola zones and porphyry roof dykes in the Harrison Pass pluton²⁶ and the numerous syn-ore dykes in the Carlin trend^{2,3} and at Cortez⁴. We emphasize that tapping of fluids from magma bodies at ~ 10 km is significantly deeper than fluid release from magmas associated with typical porphyry Cu–(Au) and associated skarn deposits, which commonly form at depths of $< \sim 4$ km (ref. 6). Shallow release of high-temperature fluids from magma bodies associated with porphyry and skarn deposits results in large temperature gradients and strong zoning patterns in metals, ore mineralogy and hydrothermal alteration. Such zoning patterns are absent in CTGDs (Table 1).

The primitive ore fluid is interpreted to have separated into immiscible brine and vapour as it ascended along a high-angle fault zone away from its source magma (Figs 2 and 3). For example, a 900°C aqueous fluid with a salinity of 10 wt% NaCl eq. that cooled adiabatically during ascent from a pressure of 300 MPa (orange arrows in Fig. 3) would have condensed a small amount of brine with a salinity of 38 wt% NaCl eq. at 690°C and 115 MPa. If vapour and brine continued to ascend and cool together, for example to 95 MPa and 653°C , 84% of the bulk fluid would be vapour with a salinity of 3.85 wt% NaCl eq. and a density of 0.34 g cm^{-3} ; the remaining 16% would be brine with a salinity of 42.9 wt% NaCl eq. and a density of 0.85 g cm^{-3} (blue arrows in Fig. 3; ref. 28; see Supplementary Note S9).

Upon fluid separation, metals would have partitioned between the vapour and brine. LA-ICP-MS analyses of both natural and synthetic fluid inclusions demonstrate significant quantities of Au, Cu, As, Sb and S can be transported by vapour, whereas Fe, Ag, Pb, Zn and Mn partition strongly into brine^{6,29} (see Supplementary Note S10). These empirical data demonstrate,

first, significant mass transport of Au by vapour and of Fe by brine, and second, separation of brine was critical to preferentially remove Fe and develop a high S/Fe ratio in the vapour that transported Au. Had abundant Fe remained in the S- and Au-bearing low-salinity vapour, pyrite would have precipitated during fluid ascent, destabilizing aqueous Au–sulphide complexes, and Au would have precipitated continuously along the fluid conduit, greatly reducing the amount of Au transported to the level of CTGDs (ref. 30). During fluid ascent and cooling, increasing differences in density would have promoted departure of the vapour from the solvus, leaving the brine at depth⁶ (green arrow in Fig. 3). We propose this rising hot Au-bearing vapour plume with a salinity of ~3–5 wt% NaCl eq. entrained meteoric water as it rose through the upper crust³¹ (light blue arrows in Fig. 3). The mixing with meteoric water (red arrows in Fig. 3) would have increased the cooling rate of the ascending plume, potentially causing the plume to pass over the critical curve (black line in Fig. 3) by near-isobaric cooling and evolve into a liquid without further phase separation³⁰ (red arrows pointing right in Fig. 3). Enthalpy–salinity relationships and calculations in conjunction with O and H isotope data from some CTGDs (ref. 1) indicate that incorporation of a reasonable quantity of meteoric water by the vapour readily produces an ore fluid of ~250 °C and ~2–3 wt% NaCl eq., consistent with upper temperatures determined for fluid inclusions in CTGDs (ref. 1; see Supplementary Note S11).

Along much of the fluid pathway, fluid acidity was probably buffered by the rock³²; however, the fluid would have evolved to become acidic at < ~350 °C owing to dissociation of carbonic acid³³ ($\text{H}_2\text{CO}_3 \Rightarrow \text{H}^+ + \text{HCO}_3^-$), probably the most important acid in the ore fluid on the basis of quadrupole mass spectrometer gas analyses of fluid inclusions in CTGDs (ref. 5; see Supplementary Note S12). The contrast between reactive carbonate rocks and overlying thrust plates of relatively impermeable, less reactive siliciclastic rocks, under hydrostatic pressure near the surface, is interpreted to have caused the now acidic ore fluid to leave high-angle fault zones and infiltrate the highly fractured carbonate country rocks at depths of <3 km. Dissolution of carbonate increased permeability, facilitating fluid flow into the country rocks and leading to further fluid–rock reaction.

Efficient gold deposition

Key to the formation of CTGDs was an effective, efficient depositional mechanism. Au occurs in arsenian and trace-element-rich pyrite in replaced wall rocks; open-space deposition of Au-bearing pyrite is rare¹, indicating that fluid–rock reaction was the main cause of Au deposition. Au-bearing pyrite occurs as rims on pre-ore pyrite, or as micrometre-scale spheroidal ‘fuzzy’ grains (Fig. 4; see Supplementary Data S2). X-ray adsorption near-edge structure, extended X-ray adsorption fine structure and secondary-ion mass spectroscopy analyses demonstrate some Au in pyrite is present as submicrometre inclusions of native Au⁰ but dominantly occurs as structurally bound Au¹⁺, which allows transport and deposition of Au by fluids that were not necessarily saturated with respect to native Au⁰ (refs 34,35). Deposition of Au was caused by reaction of reduced Au–sulphide species in the ore fluid with Fe²⁺ in the host rock to form pyrite³⁶. Loss of sulphide from the ore fluid destabilized Au–sulphide complexes and resulted in incorporation of Au and other trace metals in pyrite including primarily As, Hg, Cu, Sb, Tl and Te. Recently recognized and quantified variations in pyrite rim chemistry at the Turquoise Ridge deposit (see Supplementary Data S2) are interpreted to reflect variations in metal concentrations in the ore fluid, and zoned rims indicate that pulses of chemically distinct ore fluids delivered Au and trace metals to the deposit³⁷ (Fig. 4). The incompatible element-rich

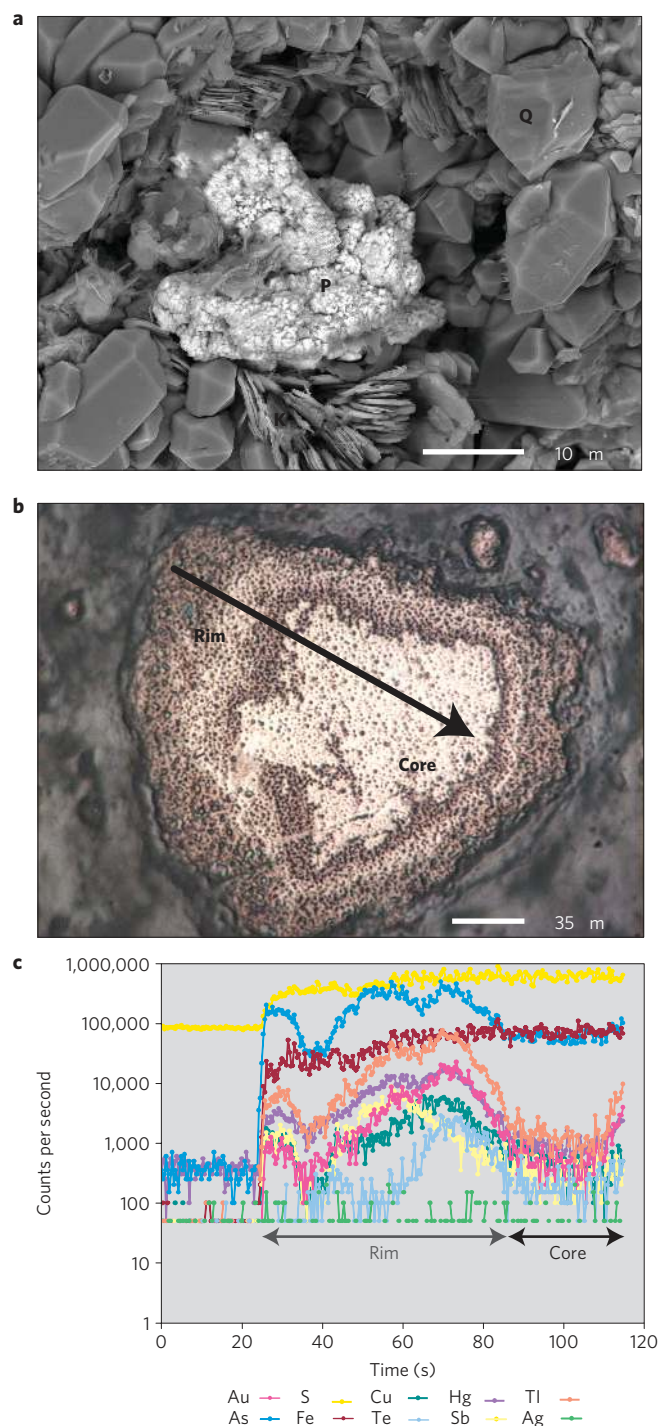


Figure 4 | Images and analyses of ore-stage pyrite. **a**, Scanning electron micrograph of ore from the Turquoise Ridge CTGD, consisting of quartz (Q), kaolinite (K) and pyrite (P). **b**, Back-scattered electron image of pyrite from Turquoise Ridge showing pre-ore core and ore-stage rim and location of LA-ICP-MS transect. **c**, Results of LA-ICP-MS transect showing a marked increase in trace elements from core to rim. Counts are directly related to concentrations of the analysed isotopes and reveal an inner rim with highest Au, Tl, Hg, Cu and Te, and a narrow outer rim with high Au, Tl, Hg, Cu and Sb.

pyrite composition reflects earlier metal partitioning between melt and the primitive ore fluid and between vapour and brine, and is consistent with vapour transport of metals. Sulphidation as the principle precipitation mechanism is supported on the scale of

individual deposits by lithogeochemical studies that indicate S was added to rock containing varying amounts of Fe (ref. 38). Ore formation was probably facilitated by extremely efficient scavenging of Au through adsorption of Au¹⁺ onto negatively charged pyrite surfaces, from acidic fluids that were undersaturated with respect to native Au⁰ (ref. 39; see Supplementary Note S13). Late-ore-stage mineralization, characterized by open-space deposition of drusy quartz, orpiment, realgar and stibnite with little to no associated Au, is best explained by cooling³⁶, which was related to the collapse of the hydrothermal system and incursion of near-surface meteoric waters.

CTGDs reflect a major thermal and mass transfer event in the Great Basin during which CTGDs formed along with other types of ore deposits including the giant Bingham Canyon porphyry Cu–Au–Mo and Mount Hope porphyry Mo deposits. The large number and variety of ore deposits that formed during this event are an indication of multiple evolutionary paths for magma and their evolved ore fluids. Such major thermal events and magma and hydrothermal fluid pathways, including the one outlined here for CTGDs, are not necessarily unique to the Great Basin. The clusters and varieties of large Neoproterozoic gold deposits in the Superior craton of eastern Canada and the Yilgarn craton of Western Australia also formed during major crustal-scale thermal events from multiple fluid pathways⁴⁰.

As the magmatic–hydrothermal processes in CTGDs are not geologically unusual, the apparent restriction of CTGDs to Nevada represents a convergence of these processes with an ideal geological setting that is specific to Nevada—that is, a deformed, carbonate-bearing, continental margin that was underlain by SCLM, which itself was modified by ~175 Myr of subduction-induced fertilization. It is this convergence that created an ideal system for the formation of CTGDs. The critical trigger was the rollback of the shallow Farallon slab that caused the asthenosphere to impinge on strongly hydrated and trace-metal-enriched SCLM, resulting in profuse magmatism. Au-bearing aqueous fluids were generated, transported, and focused into reactive carbonate wall rocks. Ore fluids dissolved and sulphidized Fe-bearing carbonate rocks, and Au adsorbed onto newly precipitated pyrite in an extremely effective depositional mechanism.

Received 17 February 2010; accepted 14 December 2010;
published online 23 January 2011

References

- Cline, J. S., Hofstra, A. H., Muntean, J. L., Tosdal, R. M. & Hickey, K. A. in *Economic Geology 100th Anniversary Volume* (eds Hedenquist, J. W., Thompson, J. F. H., Goldfarb, R. J. & Richards, J. P.) 451–484 (Society of Economic Geologists, 2005).
- Heitt, D. G., Dunbar, W. W., Thompson, T. B. & Jackson, R. G. Geology and geochemistry of the Deep Star gold deposit, Carlin trend, Nevada. *Econ. Geol.* **98**, 1107–1136 (2003).
- Ressel, M. W. & Henry, C. D. Igneous geology of the Carlin trend, Nevada: Development of the Eocene plutonic complex and significance for Carlin-type gold deposits. *Econ. Geol.* **101**, 347–383 (2006).
- John, D. A., Henry, C. D. & Colgan, J. P. Magmatic and tectonic evolution of the Caetano caldera, north-central Nevada: A tilted, mid-Tertiary eruptive center and source of the Caetano tuff. *Geosphere* **4**, 75–106 (2008).
- Cline, J. S. & Hofstra, A. H. Ore fluid evolution at the Getchell Carlin-type gold deposit, Nevada, USA. *Eur. J. Mineral.* **12**, 195–212 (2000).
- Williams-Jones, A. E. & Heinrich, C. A. Vapor transport of metals and the formation of magmatic-hydrothermal ore deposits. *Econ. Geol.* **100**, 1287–1312 (2005).
- Simon, A. C. *et al.* Gold partitioning in melt-vapor-brine systems. *Geochim. Cosmochim. Acta* **69**, 3321–3335 (2005).
- Simon, A. C., Pettke, T., Candela, P. A., Piccoli, P. M. & Heinrich, C. A. Copper partitioning in a melt-vapor-brine-magnetite–pyrrhotite assemblage. *Geochim. Cosmochim. Acta* **70**, 5583–5600 (2006).
- Simon, A. C., Pettke, T., Candela, P. A., Piccoli, P. M. & Heinrich, C. A. The partitioning behavior of As and Au in S-free and S-bearing magmatic assemblages. *Geochim. Cosmochim. Acta* **71**, 1764–1782 (2007).
- Tosdal, R. M., Wooden, J. L. & Kistler, R. W. in *Geology and Ore Deposits 2000: The Great Basin and Beyond* (eds Cluer, J. K., Price, J. G., Struhsacker, E. M., Hardyman, R. F. & Morris, C. L.) 451–466 (Geological Society of Nevada, 2000).
- Marshak, S., Karlstrom, K. & Timmons, J. M. Inversion of Proterozoic extensional faults: An explanation for the pattern of Laramide and Ancestral Rockies intracratonic deformation, United States. *Geology* **28**, 735–738 (2000).
- Emsbo, P., Groves, D. I., Hofstra, A. H. & Bierlein, F. P. The giant Carlin gold province: A protracted interplay of orogenic, basinal, and hydrothermal processes above a lithospheric boundary. *Min. Dep.* **41**, 517–525 (2006).
- Muntean, J. L., Coward, M. P. & Tarnocai, C. A. in *Deformation of the Continental Crust: The Legacy of Mike Coward 272* (eds Reis, A. C., Butler, R. W. H. & Graham, R. H.) 571–587 (Spec. Publ. Geol. Soc. Lond., 2007).
- Coney, P. J. & Reynolds, S. J. Cordilleran Benioff zones. *Nature* **270**, 403–406 (1977).
- Iwamori, H. Transportation of H₂O and melting in subduction zones. *Earth Planet. Sci. Lett.* **160**, 65–80 (1998).
- Candela, P. A. & Piccoli, P. M. in *Economic Geology 100th Anniversary Volume* (eds Hedenquist, J. W., Thompson, J. F. H., Goldfarb, R. J. & Richards, J. P.) 25–37 (Society of Economic Geologists, 2005).
- Noll, P. D., Newsom, H. W., Leeman, W. P. & Ryan, J. G. The role of hydrothermal fluids in the production of subduction zone magmas: Evidence from siderophile and chalcophile trace elements and boron. *Geochim. Cosmochim. Acta* **60**, 587–611 (1996).
- Hattori, K. H. & Guillot, S. Volcanic fronts form as a consequence of serpentine dehydration in the forearc mantle wedge. *Geology* **31**, 525–528 (2003).
- Richards, J. P. Postsubduction porphyry Cu–Au and epithermal Au deposits: Products of remelting of subduction-modified lithosphere. *Geology* **37**, 247–250 (2009).
- Humphreys, E. *et al.* How Laramide-age hydration of North American lithosphere by the Farallon slab controlled subsequent activity in the western United States. *Int. Geol. Rev.* **45**, 575–595 (2003).
- Humphreys, E. D. Post-Laramide removal of the Farallon Slab, western United States. *Geology* **23**, 987–990 (1995).
- Kelley, K. A. & Cottrell, E. Water and the oxidation state of subduction zone magmas. *Science* **325**, 605–607 (2009).
- Gans, P. B., Mahood, G. A. & Schermer, E. Synextensional magmatism in the Basin and Range province: A case study from the eastern Great Basin. (Special Paper Vol. 233, Geological Society of America 1989).
- Annen, C., Blundy, J. D. & Sparks, R. S. J. The genesis of intermediate and silicic magmas in deep crustal hot zones. *J. Petrol.* **47**, 505–539 (2006).
- Redmond, P. B., Einaudi, M. T., Inan, E. E., Landtwing, M. R. & Heinrich, C. A. Copper deposition from fluid cooling in intrusion-centered system: New insights from the Bingham porphyry ore deposit, Utah. *Geology* **32**, 217–220 (2004).
- Barnes, C. G., Burton, B. R., Burling, T. C., Wright, J. E. & Karlsson, H. R. Petrology and geochemistry of the late Eocene Harrison Pass pluton, Ruby Mountains core complex, northeastern Nevada. *J. Petrol.* **42**, 901–929 (2001).
- Henry, C. D. Ash-flow tuffs and paleovalleys in northeastern Nevada: Implications for Eocene paleogeography and extension in the Sevier hinterland, northern Great Basin. *Geosphere* **4**, 1–35 (2008).
- Driesner, T. & Heinrich, C. A. The system H₂O–NaCl. Part I: Correlation formulae for phase relations in temperature–pressure–composition space from 0 to 1000 °C, 0 to 5000 bar, and 0 to 1 X_{NaCl}. *Geochim. Cosmochim. Acta* **71**, 4880–4901 (2007).
- Seo, J. H., Guillong, M. & Heinrich, C. A. The role of sulfur in the formation of magmatic-hydrothermal copper–gold deposits. *Earth Planet. Sci. Lett.* **282**, 323–328 (2009).
- Heinrich, C. A., Driesner, T., Stefánsson, A. & Seward, T. M. Magmatic vapor contraction and the transport of gold from the porphyry environment to epithermal ore deposits. *Geology* **32**, 761–764 (2004).
- Henley, R. W. & McNabb, A. Magmatic vapor plumes and ground-water interaction in porphyry copper emplacement. *Econ. Geol.* **73**, 1–20 (1978).
- Giggenbach, W. F. Magma degassing and mineral deposition in hydrothermal systems along convergent plate boundaries. *Econ. Geol.* **87**, 1927–1944 (1992).
- Heinrich, C. A. The chemistry of hydrothermal tin–(tungsten) ore deposition. *Econ. Geol.* **85**, 457–481 (1990).
- Simon, G., Kesler, S. E. & Chrysoulis, S. Geochemistry and textures of gold-bearing arsenian pyrite, Twin Creeks, Nevada: Implications for deposition of gold in Carlin-type deposits. *Econ. Geol.* **94**, 405–422 (1999).
- Reich, M. *et al.* Solubility of gold in arsenian pyrite. *Geochim. Cosmochim. Acta* **69**, 2781–2796 (2005).
- Hofstra, A. H. *et al.* Genesis of sediment-hosted disseminated gold deposits by fluid mixing and sulfidization: Chemical-reaction-path modeling of ore-depositional processes documented in the Jerritt Canyon district, Nevada. *Geology* **19**, 36–40 (1991).
- Barker, S. L. *et al.* Uncloning invisible gold: Use of nanoSIMS to evaluate gold, trace elements and sulfur isotopes in pyrite from Carlin-type gold deposits. *Econ. Geol.* **104**, 897–904 (2009).

38. Stenger, D. P., Kesler, S. E., Peltonen, D. R. & Tapper, C. J. Deposition of gold in Carlin-type deposits: The role of sulfidation and decarbonation at Twin Creeks, Nevada. *Econ. Geol.* **93**, 210–215 (1998).
39. Widler, A. M. & Seward, T. M. The adsorption of gold(I) hydrosulfide complexes by iron sulphide surfaces. *Geochim. Cosmochim. Acta* **66**, 383–402 (2002).
40. Robert, F., Poulsen, K. H., Cassidy, K. F. & Hodgson, C. J. in *Economic Geology 100th Anniversary Volume* (eds Hedenquist, J. W., Thompson, J. F. H., Goldfarb, R. J. & Richards, J. P.) 1001–1033 (Society of Economic Geologists, 2005).

Acknowledgements

This work was supported by the National Science Foundation (EAR awards 0635657 to J.L.M., 0635658 to J.S.C. and 0609550 to A.C.S.), the US Geological Survey's Mineral

Resources External Research Program, Placer Dome Exploration and Barrick Gold Corporation.

Author contributions

J.L.M., J.S.C., A.C.S. and A.A.L. conceived the model for the CTGDs. J.L.M. took the lead in preparation of the manuscript and figures and contributed Supplementary Data S1. J.S.C. and A.A.L. contributed Supplementary Data S2 and A.C.S. contributed Supplementary Data S3.

Additional information

The authors declare no competing financial interests. Supplementary information accompanies this paper on www.nature.com/naturegeoscience. Reprints and permissions information is available online at <http://npg.nature.com/reprintsandpermissions>. Correspondence and requests for materials should be addressed to J.L.M.

Supplementary Notes

1. The range of $\delta^{34}\text{S}$ values from -4‰ to +13‰ on ore-stage pyrite includes conventional analyses of pyrite separates^{1,2} and in situ ion probe analyses. The in situ analyses^{3,4} are mainly on the lower end of the range, whereas the conventional analyses tend to be on the higher end of the range. The higher $\delta^{34}\text{S}$ values are suggestive of a sedimentary source but can be derived from magmas, if the magmas assimilated sedimentary S, as evidenced by analyses of sulfides from some Mesozoic igneous-related base metal deposits⁵ and whole rock sulfur analyses of Mesozoic and Tertiary plutons⁶ in Nevada. Conversely, $\delta^{34}\text{S}$ values near 0‰ can result from interaction of the hydrothermal fluid with rock containing diagenetic pyrite having values near 0‰, without any magmatic contribution⁷.
2. Vapor partitioning and transport of Au, Cu, As and Sb from a melt are supported by analyses of coexisting hypersaline brine and vapor-rich fluid inclusions, which represent immiscible magmatic-hydrothermal aqueous fluids trapped above 450°C and 300 bars, from porphyry copper and tin deposits. Some vapor-rich inclusions have high Au, Cu, As and Sb concentrations, sometimes higher than those in the brine⁸. Hg is a volatile element, and analyses of sublimates precipitated near active fumarole vents and sulfides in fresh pumice from Quaternary volcanoes indicate Te and Tl are also transported by magmatic vapors^{9,10}.
3. Few data document the physical state of the mass transfer from subducting oceanic lithosphere and overlying meta-sediments to the mantle wedge¹¹. Isotope evidence from some arc volcanoes is consistent with purely aqueous fluid as the medium of mass transfer¹², and data from other arc volcanoes are consistent with the medium of mass transfer being a hydrous silicate melt^{13,14}.
4. The evolution of the Au/Cu ratio of the subcontinental lithospheric mantle (SCLM) during subduction-induced magmatism and metasomatism has been modeled in published studies by using the R-factor concept^{15,16}. Arc magmatism leaves a large amount of hydrous residue in the SCLM, which due to high magmatic sulfur content likely contains some residual sulfide phases. The modeling indicates for geologically reasonable mass ratios of silicate melt to sulfide, fractionation of small amounts of sulfides from early subduction-generated magmas will leave behind a sulfide residue with relatively high Au/Cu ratios compared to the silicate melt in the rising magma. Post-subduction melting of the Au-enriched SCLM residue results in the generation of magma with a high Au/Cu ratio. This modeling assumes the sulfide-silicate melt Nernst partition coefficient for Au is greater than that for Cu in the mantle, which is supported by published sulfide:silicate melt partition coefficients that range from 15,000–19,000 for Au and ~1,400 for Cu, based on analyses of coexisting sulfide (intergrowths of Cu-Fe sulfides, pentlandite, and pyrrhotite) and MORB glass separates¹⁷.
5. The partition coefficients derived from experiments are consistent with data from the Bajo de la Alumbrera porphyry Cu-Au deposit, where sulfide melt inclusions,

- broadly FeS in composition and containing <2 ppm Au, were enriched in Cu by a factor of 10,000 compared to coexisting silicate melt inclusions¹⁸.
6. Our model is based on an aqueous fluid that evolves from magma at an oxygen fugacity of FMQ+1. This assumption is justified based on the reduced nature of the crust underlying the CTGDs in Nevada. The upper 10-15 km of crust is characterized by a thick Neoproterozoic-Paleozoic section of predominantly carbonaceous rocks that formed during Neoproterozoic rifting, formation of an early Paleozoic miogeoclinal shelf-slope sequence, and late-Paleozoic thrusting of deep-water siliciclastic rocks. The ratio of H₂S to SO₂ was calculated at FMQ+1 by using a thermodynamic model¹⁹ that calculates the fugacities of gas species in a H-O-S system. At 1000°C, the calculated sulfur species are $f_{S_2} = 0.001$ bar; $f_{H_2S} = 10$ bars and $f_{SO_2} = 0.032$ bar, yielding a fugacity ratio for H₂S/SO₂ of ~300. We note that the published thermodynamic model results are consistent with an independent calculation²⁰ of the proportion of sulfide (H₂S) to sulfate (SO₂) in magmatic aqueous fluid determined by using thermochemical data from the JANAF database²¹ and fugacity coefficients²² that yield a calculated H₂S/(H₂S + SO₂) ratio of approximately 0.95 at 1000°C. It is important to recognize that at more oxidizing conditions, as the oxygen fugacity increases from FMQ+1 to FMQ+2.5, the ratio of H₂S to SO₂ decreases^{23,24} and at FMQ+2.5 the sulfur budget is dominated by sulfate (SO₂). Thus, our model is specific with respect to the oxygen fugacity of the ore fluid.
 7. Based on experiments^{25,26} and analyses of gases from active volcanoes^{27,28} and melt inclusions^{29,30}, intermediate to felsic magmas release volatiles that are dominantly H₂O with minor CO₂ with much less S-bearing and other gases. A rhyolitic melt at 1000°C, containing 6 wt% H₂O, will release an aqueous phase at 230 MPa; however, addition of 1000 ppm CO₂ increases the saturation pressure to 400 MPa³¹. The released volatile phase will initially be CO₂-rich (initial CO₂/H₂O up to 0.8), but will progressively become more H₂O-rich with continued devolatilization³¹.
 8. In addition to the Cu partitioning experiments, new experimental data indicate Au concentrations in H₂S-dominant fluids at 1000°C, 150 MPa and 3 wt% NaCl eq. may range from 4 to 7 ppm and even higher in fluids containing KCl²⁰. The results indicate Au transport would be enhanced in fluids released from the high-K Eocene magmas in Nevada.
 9. Adiabatic cooling paths were calculated using a specific heat ratio of 1.25 (pure H₂O at 1000°C). The relative masses and salinities of coexisting vapor and brine along the two-phase surface in the NaCl-H₂O system were calculated using software developed by T. Driesner (www.igmr.ethz.ch/people/td/sowat) based on published correlation formulae in P-T-X space³². The addition of CO₂ enlarges the solvus to higher pressures and temperatures. For example, addition of 5 mol % CO₂ increases the pressure of the solvus approximately 0.1 MPa at a given temperature and bulk salinity.
 10. Experiments using synthetic fluid inclusions at 800°C show partition coefficients for Au between the vapor and brine ($D^{v/b}$) ranging from 0.17 at 110 MPa to 0.72 at 145 MPa³³, which contrast with data from natural systems that suggest that $D^{v/b}$ is sometimes greater than one⁸. Nevertheless, because the vapor comprises most

- of the mass of the bulk fluid, it will transport the majority of the Au. Experimentally derived partition coefficients for Fe ($D^{v/b}$) at 800°C range from 0.05 at 100 MPa to 0.5 at 145 MPa³⁴.
11. The δD of magmatic vapor ranges from -10 to -30‰ based on analyses of volcanic gases³⁵ (see Supplementary Data 1). The δD of Eocene meteoric water is estimated to be -130 to -175‰ (see Supplementary Data 1). The δD of fluid inclusions in ore-stage quartz at the Getchell deposit ranges from -84 to -114‰³⁶, which corresponds to mixture of 2 parts meteoric water and 1 part magmatic vapor. From these data, 1 part magmatic vapor with 3.85 wt% NaCl eq. at 450°C and 50 MPa was mixed with 2 parts meteoric water with a salinity of 1.5 wt% NaCl eq. at 150°C (based on a geothermal gradient of 30°C/km and 5 km depth), utilizing enthalpy-chloride relationships, to yield a 250°C fluid with a salinity of 2.6 wt% NaCl eq.³⁷
 12. Possible magmatic-hydrothermal alunite has only been reported from one altered dike at the Beast deposit on the Carlin trend³⁸, and H₂S is the dominant sulfur species that has been detected in quadrupole mass spectrometer gas analyses of fluid inclusions in CTGDs in Nevada^{36,39}. The lack of alunite and the predominance of reduced sulfur in the ore fluids argue against oxidized sulfur as the source of acidity. Interaction of fluids with rocks during long transport of fluids from mid-crustal magma chambers to within a few kilometers of the surface would have reduced oxidized sulfur species and converted HCl in the fluids to alkali chlorides³⁵. In addition, much of Paleozoic stratigraphy that comprises a large portion of the upper crust in northern Nevada consists of carbonaceous carbonate and siliciclastic rocks, which would have facilitated reduction of the ascending ore fluids. Quadrupole mass spectrometer gas analyses of fluid inclusions shows CO₂ is the dominant gaseous species, occurring at concentrations of 2-4 mol %^{36,39}. Other gases present include CH₄ (<0.4 mol %) and H₂S (10⁻¹–10⁻² m). Though not as strong as sulfuric or hydrochloric acid, dissociation of carbonic acid at low temperatures can result in kaolinite-stable alteration. Simple equilibrium and reaction path models show that reaction of a fluid at 200°C with 4 mol %t CO₂ with carbonate will decrease pH to 4.3-4.5. Following carbonate dissolution, the pH decreases to 3-3.5 where kaolinite is stable³⁹. Kaolinite±dickite-bearing alteration at depths of a kilometer occurs along the low-temperature (~150°C) fringes of upwelling zones in the Broadlands-Ohaaki geothermal system in New Zealand and results from the disassociation of carbonic acid in steam-heated geothermal fluids containing 0.5 mol % CO₂^{40,41}.
 13. Experiments at 25°C showed adsorption of gold from solutions undersaturated with respect to native gold by pyrite at pH values <5.5 was 100%⁴². The main gold complex adsorbed was AuHS°.

References

1. Hofstra, A. H. & Cline, J. S. Characteristics and models of Carlin-type gold deposits. *Gold in 2000*, (eds. Hagemann, S. G. & Brown, P. E.) Reviews in Economic Geology **13**, 163-220 (2000).
2. Emsbo, P., Hofstra, A. H., Lauha, E. A., Griffin, G. L. & Hutchinson, R. W. Origin of high-grade gold ore, source of ore fluid components, and genesis of the

3. Cline J. S. *et al.* Multiple sources of ore-fluid components at the Getchell Carlin-type gold deposits, Nevada, USA. *Mineral Exploration and Sustainable Development* (eds. Eliopoulos, D. *et al.*) **2**, 965-968 (2003).
4. Kesler, S. E., Ye, A., Fortuna, J. & Riciputi, L. Evidence for magmatic input to Carlin-type deposits. *Mineral Exploration and Sustainable Development* (eds. Eliopoulos, D. *et al.*) **1**, 493-494 (2003).
5. Vikre, P. G. Subjacent crustal sources of sulfur and lead in eastern Great Basin metal deposits. *G.S.A. Bull.* **112**, 764-782 (2000).
6. DeYoung, S., Arehart, G. & Poulson, S. Sulfur isotope constraints on plutonic rocks of the Great Basin; implications for magma-crust interaction and crustal architecture. Geological Society of America Abstracts with Programs, **37**, 358, (2005).
7. Hofstra, A. H., Christiansen, W. D. & Tousignant, G. Lithogeochemistry of the Devonian Popovich Formation in the northern Carlin Trend. Geological Society of Nevada 2010 Symposium Program with Abstracts, 53, (2010).
8. Williams-Jones, A. E. & Heinrich, C. A. Vapor transport of metals and the formation of magmatic-hydrothermal ore deposits. *Econ. Geol.* **100**, 1287-1312 (2005).
9. Fulignati, P. & Sbrana A. Presence of native gold and tellurium in the active high-sulfidation hydrothermal system of the La Fossa volcano (Vulcano, Italy). *J. Volc. Geotherm. Res.* **86**, 187-198 (1998).
10. Larocque, A. C. L. *et al.* Deposition of a high-sulfidation Au assemblage from a magmatic volatile phase, Volcán Popocatepetl, Mexico. *J. Volc. Geotherm. Res.* **170**, 51-60 (2008).
11. Manning, C.E. The chemistry of subduction-zone fluids. *Earth and Planetary Scienc Letters*, **223**, 1-16 (2004).
12. Duggen, S., Portnyagin, M., Baker, J., Ulfbeck, D., Hoernle, K. Garbe-Schonberg, D. & Grassineau, N. Drastic shift in lava geochemistry in the volcanic-front to rear-arc region of the Southern Kamchatkan subduction zone: Evidence for the transition from slab surface dehydration to sediment melting. *Geochim. Cosmochim. Acta* **71**, 452-480 (2007).
13. Plank, T. Constraints from thorium/lanthanum on sediment recycling at subduction zones and the evolution of the continents. *J. Petrol.*, **46**, 921-944 (2005).
14. Plank, T. & Langmuir, C.H. The chemical composition of subducting sediment and its consequences for the crust and mantle. *Chem. Geol.*, **145**, 325-394 (1998).
15. Richards, J. P. Postsubduction porphyry Cu-Au and epithermal Au deposits: Products of remelting of subduction-modified lithosphere. *Geology* **37**, 247-250 (2009).
16. Campbell, I. H. & Naldrett, A. J. The influence of silicate:sulfide ratios on the geochemistry of magmatic sulfides. *Econ. Geol.*, **74**, 1503-1506 (1979).
17. Peach, C. L., Mathez, E. A. & Keays, R. R. Sulfide melt-silicate melt distribution coefficients for noble metals and other chalcophile elements as deduced from

- MORB: Implications for partial melting. *Geochim. Cosmochim. Acta* **54**, 3379-3389 (1990).
18. Halter, W. E. Heinrich, C. A. & Petke, T. Magma evolution and the formation of porphyry Cu-Au ore fluids: Evidence from silicate and sulfide melt inclusions. *Min. Dep.* **39**, 845-863 (2005).
 19. Clemente, B. A., Scaillet, B. & Pichavant, M. The solubility of sulfur in hydrous rhyolitic melts. *J. Petrol.* **45**, 2171-2196 (2004).
 20. Zajacz, Z. et al. Alkali metals control the release of gold from volatile-rich magma. *Earth Planet. Sci. Lett.* **297**, 50-56 (2010).
 21. Chase, M. W., Davis, C. A., Downey, J. R., Frurip, D. J., McDonald, R. A. & Syverud, A. N. JANAF thermochemical tables – 3rd edition. 1. Al-Co. *J. Phys. Chem. Ref. Data* **14**, 1-926 (1985).
 22. Churakov, S. V. & Gottschalk, M. Perturbation theory based equation of state for polar molecular fluids: II. Fluid mixtures. *Geochim. Cosmochim. Acta*, **67**, 2415-2425 (2003).
 23. Jugo, P. Sulfur content at sulfide saturation in oxidized magmas. *Geology*, **37**, 415-418 (2009).
 24. Jugo, P., Luth, R. & Richards, J. Experimental data on the speciation of sulfur as a function of oxygen fugacity in basaltic melts. *Geochim. Cosmochim. Acta*, **69**, 497-503 (2005).
 25. Candela, P. A. & Piccoli, P. M. Model ore-metal partitioning from melts into vapor and vapor/brine mixtures. *Magmas, Fluids, and Ore Deposits* (ed. Thompson, J. F. H.) 101-128 (Mineralogical Association of Canada Short Course Series, 1995).
 26. Webster, J. D. & Mandeville, C. W. Fluid immiscibility in volcanic environments. *Fluid-Fluid Interactions* (eds. Liebscher, A. & Heinrich, C. A.) 313-362 (Mineralogical Society of America/Geochemical Society, Reviews in Mineralogy and Geochemistry, vol. 65, 2007).
 27. Symonds, R. B., Reed, M. H. & Rose, W. I. Origin, speciation, and fluxes of trace element gases at Augustine Volcano, Alaska; insights into magma degassing and fumarolic processes. *Geochim. Cosmochim. Acta* **56**, 633-657 (1992).
 28. Fischer, T. P., Arehart, G. B., Sturchio, N. C. & Williams, S. N. The relationship between fumarole gas composition and eruptive activity at Galeras Volcano, Columbia. *Geology* **24**, 531-534 (1996).
 29. Blundy, J. & Cashman, K. Petrologic reconstruction of magmatic system variables and processes. *Mineral, Inclusions and Volcanic Processes* (eds. Putirka, K. D. & Tepley, F. J.) 179-239 (Mineralogical Society of America/Geochemical Society, Reviews in Mineralogy and Geochemistry, vol. 69, 2008).
 30. Metrich, N. & Wallace, P. J. Volatile abundances in basaltic magmas and their degassing paths tracked by melt inclusions. *Mineral, Inclusions and Volcanic Processes* (eds. Putirka, K. D. & Tepley, F. J.) 363-402 (Mineralogical Society of America/Geochemical Society, Reviews in Mineralogy and Geochemistry, vol. 69, 2008).

31. Newman, S. & Lowenstern, J. B. VOLATILECALC: A silicate melt-H₂O-CO₂ solution model written in Visual Basic for excel. *Comput. Geosciences* **28**, 597-604 (2002).
32. Driesner, T. & Heinrich, C. A. The system H₂O-NaCl. Part I: Correlation formulae for phase relations in temperature-pressure-composition space from 0 to 1000°C, 0 to 5000 bar, and 0 to 1 X_{NaCl}. *Geochim. Cosmochim. Acta* **71**, 4880-4901 (2007).
33. Simon, A. C. *et al.*, Gold partitioning in melt-vapor-brine systems. *Geochim. Cosmochim. Acta* **69**, 3321-3335 (2005).
34. Simon, A. C., Pettke, T., Candela, P. A., Piccoli, P. M. & Heinrich, C. A. Magnetite solubility and iron transport in magmatic-hydrothermal environments. *Geochim. Cosmochim. Acta* **68**, 4905-4914 (2004).
35. Giggenbach, W. F. Magma degassing and mineral deposition in hydrothermal systems along convergent plate boundaries. *Econ. Geol.* **87**, 1927-1944 (1992).
36. Cline, J. S. & Hofstra, A. H. Ore fluid evolution at the Getchell Carlin-type gold deposit, Nevada, USA. *Eur. J. Mineral.* **12**, 195-212 (2000).
37. Tanger, J. C. & Pitzer, K. S. Thermodynamics of NaCl-H₂O; a new equation of state for the near-critical region and comparisons with other equations for adjoining regions. *Geochim. Cosmochim. Acta* **53**, 973-987 (1989).
38. Ressel, M. W., Noble, D. C., Henry, C. D. & Trudel, W. S. Dike-hosted ores of the Beast deposit and the importance of Eocene magmatism in gold mineralization of the Carlin trend, Nevada. *Econ. Geol.*, **95**, 1417-1444 (2000).
39. Cline, J. S., Hofstra, A. H., Muntean, J. L., Tosdal, R. M. & Hickey, K. A. Carlin-type gold deposits in Nevada, USA: Critical geologic characteristics and viable models. *Economic Geology 100th Anniversary Volume* (eds. Hedenquist, J. W., Thompson, J. F. H., Goldfarb, R. J. & Richards, J. P.) 451-484 (Society of Economic Geologists, Littleton, CO, 2005).
40. Hedenquist, J. W. The thermal and geochemical structure of the Broadlands-Ohaaki geothermal system, New Zealand. *Geothermics*, **19**, 151-185 (1990).
41. Simmons, S. F. & Browne, P. R. L. Hydrothermal minerals and precious metals in the Broadlands-Ohaaki geothermal system: implications for understanding low-sulfidation epithermal environments. *Econ. Geol.*, **95**, 971-999 (2000).
42. Widler, A. M. & Seward, T. M. The adsorption of gold(I) hydrosulfide complexes by iron sulphide surfaces. *Geochim. Cosmochim. Acta* **66**, 383-402 (2002).

Supplementary Data 1

Review of Hydrogen and Oxygen Isotopic Data

Figure 1 summarizes published H and O isotope compositions of hydrothermal fluids most closely associated with formation of Au-bearing pyrite in CTGDs, assuming a temperature of 200°C. The data were generated from analyses of quartz (O isotopes) of replacement origin (jasperoid) that hosts Au-bearing pyrite, fluid inclusions within that quartz (H isotopes), and hydrothermal kaolinite within ore zones (H and O isotopes). Analyses of illite and muscovite were not included because, unlike kaolinite, these minerals are predominantly pre-ore.

Note the traditional primary magmatic water box¹ is not shown in Figure 1. Instead, a box showing the range of hydrogen and oxygen isotopic compositions of water dissolved in silicic magmas prior to fluid release is shown (box labeled “H₂O in Felsic Magmas” in Fig. 1)^{2–5}. Also shown is the range of compositions for magmatic vapors discharged from active arc volcanoes (box labeled “High-Temp Vapors” in Fig. 1)⁶. The bulk fractionation for deuterium between released H₂O and vapor-saturated magma can vary between 0 and 40‰^{3–4}. Thus, as water exsolves from a vapor-saturated melt, the residual H₂O in the melt will become progressively more depleted in deuterium (“degassing trend” in Fig. 1). For example, igneous biotite can have δD values as low as -120‰ because of this degassing^{5,7}. Therefore, water released from magmas can show a wide variation in deuterium composition ranging from -10‰ to -120‰⁵.

The δD of Eocene meteoric waters in northern Nevada has been previously estimated to be in the range of -110 to -160‰⁸; however, the higher end of this range is mainly based on analyses of hydrothermal kaolinite in CTGDs, and the assumption that the kaolinite formed entirely from meteoric waters. We conclude that the δD value of Eocene meteoric water during formation of CTGDs was <-130‰, and that higher δD values are consistent with contributions from magmatic fluids, based on the following analysis of published data. δD values of supergene alunite from various CTGDs range from -120‰ to -159‰⁹. However, the oldest dated supergene alunite (26 Ma), for which there is δD data, has a value of -131‰⁹. δD values of supergene kaolinite from the Betze-Post deposit range from -121‰ to -143‰; however, the age of the supergene kaolinite is unknown and dates of supergene alunite from Post-Betze range from 8 to 10 Ma⁹, much younger than the deposit. Significantly, fluid inclusions in late ore-stage realgar from Getchell and drusy quartz from the Carlin trend and Jerritt Canyon have δD and $\delta^{18}O$ values near the meteoric water line; the δD values of these analyses range mainly between -130‰ and -155‰¹⁰.

Figure 1 shows that δD values for water from the ore-forming stage in CTGDs range from -33‰ to -175‰ and lie along a mixing trend between high-temperature magmatic vapors and exchanged meteoric waters. The higher δD_{H_2O} values that are consistent with magmatic fluids come from the Getchell¹¹, Turquoise Ridge¹², and Twin Creeks deposits in the Getchell district and the Deep Star deposit¹³ on the Carlin trend. The highest δD_{H_2O} values from Deep Star are from kaolinite in high-grade ore along the Hanging Wall Fault in the center of the deposit, whereas the lower δD values come from ore along the margin of the deposit¹³. However, subsequent analyses from Deep Star ore showed that δD_{H_2O} values of >-105‰ occurred in clay separates that had greater amounts

of white mica and smectite than kaolinite, whereas separates that were dominantly kaolinite had δD_{H_2O} values $< -110\text{‰}$ ¹⁰. The authors of the original Deep Star analyses¹³ maintain that X-ray diffraction analyses of their clay separates yielded only kaolinite and quartz peaks, with no evidence of contamination by white mica or smectite¹⁴. We conclude that the δD_{H_2O} values of inclusion fluids and kaolinite in Figure 1 indicate varying degrees of mixing between exsolved magmatic vapor and exchanged meteoric water. The strongest evidence for the involvement of magmatic fluids is provided by fluid inclusion data from the Getchell and Turquoise Ridge deposits. The mixing trend is further defined by data from other CTGDs including data from Carlin trend, Jerritt Canyon, and Alligator Ridge deposits that have δD_{H_2O} values as high as -105‰ , suggesting the ore fluid was predominantly, but not necessarily entirely, meteoric water.

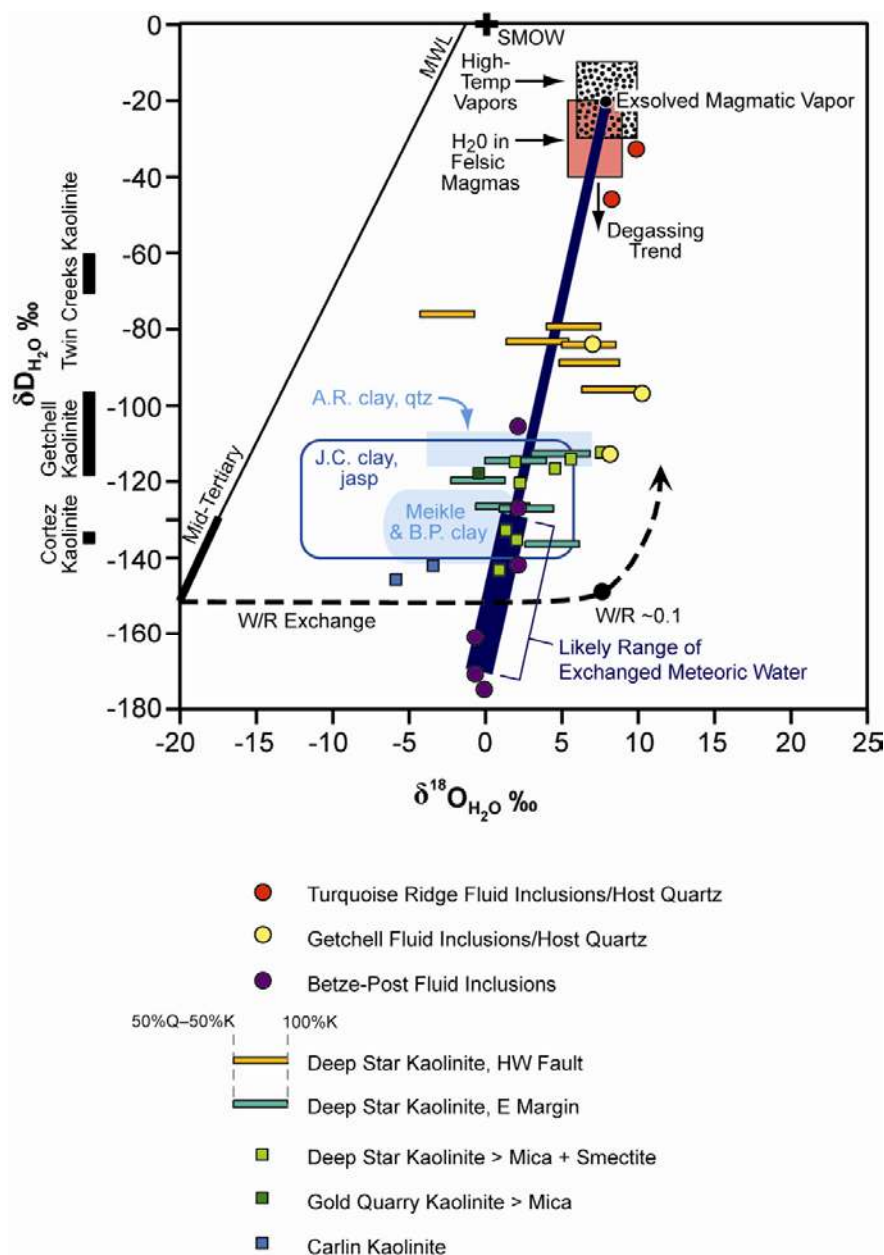


Figure 1. Hydrogen and O isotope compositions of ore-stage hydrothermal fluids in CTGDs, calculated for 200°C, relative to meteoric water (MWL), ocean water (SMOW), vapor-saturated felsic magmas³⁻⁵, and high-temperature vapors released from magmas^{4,6}. Fluid inclusion (δD) and host quartz ($\delta^{18}O$) analyses are from the Turquoise Ridge¹², Getchell¹¹, and Betze-Post deposits¹⁵. Waters calculated from kaolinite analyses (either δD or δD and $\delta^{18}O$) are from the Cortez¹⁶, Getchell¹⁰, Twin Creeks¹⁰, Deep Star (bars¹³, squares¹), Gold Quarry¹⁰ and Carlin deposits¹⁷. The Deep Star analyses marked by the bars reflect quartz impurities. The bars are tie lines that reflect water in equilibrium with 100% kaolinite (right end of the bar) to 50% quartz-50% kaolinite (left end of the bar). The blue regions and outlines represent ranges of values calculated from analyses of coexisting clay (δD) and quartz ($\delta^{18}O$) from the Jerritt Canyon^{8,10,18}, Alligator Ridge¹⁹⁻²⁰, Meikle and Betze-Post deposits (Meikle & B.P.)^{9,21}. The dashed line represents the trend of meteoric water evolution during water:rock interaction at progressively lower water:rock ratios (calculated for 200°C). The blue line represents a mixing line between released magmatic vapors and exchanged meteoric water, shown as a δD range from -130‰ to -175‰. The heavy black line along the meteoric water line shows the estimated value of Eocene meteoric waters. See text for discussion.

References

1. Taylor, H. P., Jr. Oxygen isotope studies of hydrothermal mineral deposits. in *Geochemistry of Hydrothermal Ore Deposits* (ed. H. L. Barnes) 109-142 (Holt, Rinehart & Winston, New York, 1967).
2. Taylor, B. E., Eichelberger, J.C. & Westrich, H. R., Hydrogen isotopic evidence of rhyolitic magma degassing during shallow intrusion and eruption. *Nature* **306** 541-545 (1983).
3. Dobson, P. F., Epstein, S. & Stolper, E. M. Hydrogen isotope fractionation between coexisting vapor and silicate glasses and melts at low pressure. *Geochim. Cosmochim. Acta* **53**, 2723-2730 (1989).
4. Taylor, B. E. Degassing of H₂O from rhyolite magma during eruption and shallow intrusion, and the isotopic composition of magmatic water in hydrothermal systems. in *Magmatic Contributions to Hydrothermal Systems* (ed. J. W. Hedenquist) 190-194 (Geological Survey of Japan, Report 279, 1992).
5. Hedenquist, J. W. & Richards, J. P. The influence of geochemical techniques on the development of genetic models for porphyry copper deposits. in *Techniques in Hydrothermal Ore Deposits Geology* (eds. Richards, J. P. & Larson, P. B.) 235-256 (Reviews in Economic Geology, Vol. 10, Society of Economic Geologists, Littleton, CO, 1998).
6. Giggenbach, W. F. Magma degassing and mineral deposition in hydrothermal systems along convergent plate boundaries. *Econ. Geol.* **87**, 1927-1944 (1992).
7. Sheppard, S. M. F. & Taylor, H. P., Jr. Hydrogen and oxygen isotope evidence for the origins of water in the Boulder batholith and the Butte ore deposits. *Econ. Geol.* **69**, 926-946 (1974).
8. Hofstra, A. H. *et al.* Age constraints on Jerritt Canyon and other Carlin-type gold deposits in the western United States – relationship to mid-Tertiary extension and magmatism. *Econ. Geol.* **94**, 769-802 (1999).
9. Arehart G. B., Kesler, S. E., O'Neil, J. R. & Foland, K. A. Evidence for the supergene origin of alunite in sediment-hosted micron gold deposits, Nevada. *Econ. Geol.* **87**, 263-270 (1992).
10. Cline, J. S., Hofstra, A. H. Muntean, J. L., Tosdal, R. M. & Hickey, K. A. Carlin-type gold deposits in Nevada, USA: Critical geologic characteristics and viable models. in *Economic Geology 100th Anniversary Volume* (eds. Hedenquist, J. W., Thompson, J. F. H., Goldfarb, R. J. & Richards, J. P.) 451-484 (Society of Economic Geologists, Littleton, CO, 2005).
11. Cline, J. S. & Hofstra, A. H. Ore fluid evolution at the Getchell Carlin-type gold deposit, Nevada, USA. *Eur. J. Mineral.* **12**, 195-212 (2000).
12. Shigehiro, M. Mineral paragenesis and ore fluid at the Turquoise Ridge gold deposit, Nevada. (unpub. M.S. thesis, University of Nevada Las Vegas, 152 p., 1999).
13. Heitt, D. G., Dunbar, W. W., Thompson, T. B. & Jackson, R. G. Geology and geochemistry of the Deep Star gold deposit, Carlin trend, Nevada. *Econ. Geol.* **98**, 1107-1136 (2003).
14. Thompson, T. B., personal communication (2010).

15. Lubben, J. D. Silicification across the Betze-Post Carlin-type Au deposit: clues to ore fluid properties and sources, northern Carlin trend, Nevada. (unpub. M.S. thesis, University of Nevada Las Vegas, 155 p., 2004).
16. Rye, R. O., Doe, B. R. & Wells, J. D. Stable isotope and lead isotope study of the Cortez, Nevada, gold deposit and surrounding area. *U.S.G.S. Jour. of Res.* **2**, 13-23, (1974).
17. Kuehn, C. A. Studies of disseminated gold deposits near Carlin, Nevada: evidence of a deep geologic setting of ore formation. (unpub. Ph.D. thesis, Pennsylvanian State University, 395 p., 1989).
18. Hofstra, A. H., Geology and genesis of the Carlin-type gold deposits in the Jerritt Canyon district, Nevada. (unpub. Ph.D. thesis, University of Colorado, 719 p., 1994).
19. Ilchik, R. P. Geology and geochemistry of the Vantage gold deposits, Alligator Ridge-Bald Mountain mining district, Nevada. *Econ. Geol.* **85**, 50-75 (1990).
20. Nutt, C. J. & Hofstra, A.H. Alligator Ridge: a shallow Carlin-type gold district. *Econ. Geol.*, **98**, 1225-1241 (2003).
21. Emsbo P., Hofstra, A. H., Lauha, E. A., Griffin, G. L. & Hutchinson, R. W. Origin of high-grade gold ore, source of ore fluid components, and genesis of the Meikle and neighboring Carlin-type deposits, Northern Carlin Trend, Nevada. *Econ. Geol.*, **98**, 1069-1100 (2003).

Supplementary Data 2

Methodology for EPMA Analyses of Pyrite

Pyrites from the Carlin-type Turquoise Ridge gold deposit in the Getchell district in northern Nevada were analyzed by using a JEOL electron probe microanalyzer JXA-8900 (EPMA) at the University of Nevada Las Vegas Electron Microanalysis and Imaging Laboratory operated with the following probe conditions (Table 1): 1) accelerating voltage of 20 kV, 2) beam current of 10 nA for major elements and 100nA for trace elements, and 3) a beam diameter of 2 μ m. A suite of major and trace elements (Table 2) designed to identify chemical patterns in pyrite in the Getchell district was used in the analyses and measured simultaneously by using four wavelength dispersive (WDS) X-ray spectrometers (Table 1). The X-ray line, spectrometer, and calculated 3-sigma minimum detection limit in ppm and wt% are listed in Table 2 for each element. Total time per spot analysis is 6 minutes for major elements and 35 minutes for the trace elements using the format for the Getchell suite of elements in Table 2. The lengthy analysis times are due to the extended counting times required to achieve low detection limits on Au.

Major elements (Fe, S, As; Table 2) were first analyzed at low current (10 nA) and trace level elements were subsequently analyzed (Au, Tl, etc.; Table 2) at higher current (100 nA) on the same location. Both Si and Ca were analyzed to evaluate the contamination of quartz and calcite from the ground mass. Experiments on the Turquoise Ridge pyrites using the operating conditions discussed above indicate that both S and Hg remained stable under the above operating conditions for the duration of the analysis. Other experiments show that above 125 nA, Hg diffusion becomes significant resulting in low mercury concentrations. The Au $L\alpha$ peak position is 88.65 nm with no interference from other element peak positions; however, detection limits increase to 90-125 ppm. Alternatively, a setup using the Au $M\alpha$ peak position yields detection limits <70ppm, but there is an unavoidable interference from Fe that yields erroneously high concentrations of Au. Therefore, the best option is to sacrifice the detection limit by using the Au $L\alpha$ peak. Sean Mulcahy and Aaron Bell are acknowledged for their assistance in developing the EPMA technique for pyrite analyses.

EPMA analyses are presented in Table 3 for both cores and rims from three separate pyrite grains that represent the chemistry of the pyrites from each of the three zones named the “High Grade Bullion” (HGB), the “148”, and the “Better Be There” (BBT) at Turquoise Ridge. Figure 1 shows the typical textures of pyrite at Turquoise Ridge.

Supplementary Data 3

Experimental constraints on Cu and Au partitioning between monosulfide solid solution and silicate melt

Experiments were performed to quantify the partitioning of Au and Cu between monosulfide solid solution (mss) and silicate melt at a higher sulfur fugacity than previously determined¹. In this Electronic Supplement we describe the experimental and analytical procedures and present Nernst-type partition coefficients for Au and Cu between mss and melt.

Experimental Procedures

A synthetic, hydrous haplogranite glass (Corning CGM-3) was used as the starting melt composition. The starting glass composition in wt. % oxides is: SiO₂ 72.72; Al₂O₃ 11.84, K₂O 4.50, Na₂O 4.00, CaO 0.05, Fe₂O₃ 0.03, MnO 0.01, MgO 0.01, TiO₂ 0.01. Pyrrhotite (Santa Eulalia, AMNH catalog number 52603; the starting pyrrhotite transforms to monosulfide solid solution (mss) at run conditions) and Sudbury chalcopyrite (ccp; this phase transforms to intermediate solid solution (iss) at run conditions) obtained from the American Museum of Natural History (AMNH catalog number 52407), and magnetite (mt) from Cornwall, Pennsylvania were used in the experiments. X-ray diffraction (XRD) and wavelength dispersive spectrometry (WDS) - electron probe microanalysis (EPMA) were used to characterize the mt, iss and mss, and laser ablation inductively coupled plasma mass spectrometry (LA-ICP-MS) also was used to characterize the starting mss and ccp. The mt is end-member magnetite, ($a_{\text{Fe}_3\text{O}_4}^{\text{mt}} \approx 1$). The mss has the composition $\text{Fe}_{(0.950 \pm 0.009)}\text{S}$, and contains approximately 250 $\mu\text{g/g}$ Cu. The iss has the composition $\text{Cu}_{(1.045 \pm 0.008)}\text{Fe}_{(0.991 \pm 0.009)}\text{S}_2$. An aqueous solution containing 10 wt. % NaCl eq., was prepared by dissolving equi-molar proportions of reagent grade NaCl, KCl and HCl into 18 milliohms ($\text{m}\Omega$) laboratory water. Copper(I) chloride (reagent grade, >99.9 % Cu) was added to the starting aqueous solution to yield a final Cu concentration of 5 mg/g. At run conditions the aqueous fluid is single phase^{2,3}.

Gold capsules (4.8 mm ID, 5 mm OD, 30 mm length) were loaded with approximately 20 mg mt, 20 mg ccp, 20 mg po, 40 mg rhyolite, and 100 μL aqueous solution. Capsules were placed inside cold-seal René-41 pressure vessels and the system was pressurized by using water as the pressure medium. Charges were pressurized at ambient temperature to approximately 50 MPa and heated to 800°C while left open to a pressure reservoir. The pressure during heating climbed to close to the final run pressure of 150 MPa. Once the desired temperature was reached, pressure was increased to and maintained at 150 ± 2 MPa for the life of each run. Pressure was measured by using a factory-calibrated Heise gauge. The center of the charge corresponds to the hotspot inside the vessel and the temperature gradient across the charge is 1.7°C/cm. Experiments were quenched isobarically along a two-stage cooling path involving air stream cooling from 800°C to 200°C followed by immersion of the vessel into an ambient-temperature water bath. Capsules were removed from the vessels, cleaned, examined microscopically, weighed to verify mechanical integrity at run conditions, and opened to remove the run products. Experiments were considered successful if the mass of the capsule changed by no more than 0.3 mg and the phase assemblage Iss-Mss-Mt-glass was present.

In all assemblages, f_{O_2} was imposed by thermal dissociation of the water pressure medium and reaction of O_2 with the Ni-based (53 wt. % Ni) René-41 pressure vessel via the following equilibria:



The value for f_{O_2} was measured by using the hydrogen sensor technique (Ag-AgCl; H_2O -AgCl)⁴. The determined value was $\log f_{O_2} = -14 \pm 1$ (~FMQ+1). The f_{S_2} , at a fixed f_{O_2} , was controlled by using the assemblage iss-mss-mt. We calculated f_{S_2} by using an empirical model⁵ that calculates values for f_{S_2} by simultaneously determining the values for f_{O_2} , f_{H_2} , f_{H_2S} , and f_{SO_2} , all of which are related to one another via the following equilibria:



and



The calculated value for f_{S_2} is 0.6 bars. The calculated ratio of H_2S/SO_2 is ~300.

Analytical Procedures

Silicate glass from each experiment was analyzed by using WDS-EPMA following published suggestions⁶⁻⁷. EPMA conditions for major elements were: a 15 micron defocused beam, 15 kV accelerating potential and a 5 nA beam current with a minimum counting time of twenty seconds (sum of peak and background). We quantified S by using a 10 micron beam, a 30 kV acceleration voltage, a 50 nA Faraday cage current. Cu and Au in silicate glasses were quantified by using LA-ICP-MS; NBS-610 was used as the reference silicate glass standard and the Si concentrations of glass, determined by WDS-EPMA, was used as the internal standard to calculate absolute concentrations. Published LA-ICPMS settings and methodology were followed⁸⁻¹³. Recovered mss crystals were characterized compositionally by using WDS-EPMA and the following analytical conditions: a 15 micron beam diameter, a 30 kV accelerating potential and a 30 nA beam current. We used $K\alpha$ X-ray emission line for Cu and $L\alpha$ X-ray emission line for Au.

Results

The average element concentrations, in wt. % oxides, for experimental glasses ($\pm 2\sigma$) are: SiO_2 71.89 (0.46); Al_2O_3 11.50 (0.33), K_2O 5.28 (0.28), Na_2O 3.26 (0.18), FeO 0.71 (0.21). The average concentrations ($\pm 2\sigma$) of Cu and Au in the recovered silicate glasses are 9 (1.5) $\mu g/g$ and 0.37 (0.4) $\mu g/g$, respectively. The concentrations ($\pm 2\sigma$) of Cu and Au in recovered mss are 32,500 (14,000) $\mu g/g$ and 181 (70) $\mu g/g$, respectively. The concentrations of Cu and Au in recovered silicate glass and mss were used to calculate Nernst partition coefficients mss and melt as

$$D_i^{mss/melt} = C_i^{mss} / C_i^{melt} \quad (5)$$

where C_i^j is the concentration of Cu or Au in phase j where j represents mss or melt. The calculated value for $D_{Cu}^{mss/melt}$ is 3600 and for $D_{Au}^{mss/melt}$ ($\pm 1\sigma$) is 490.

References

1. Jugo, P.J., Candela, P.A. and Piccoli, P.M. Magmatic sulfides and Au:Cu ratios in porphyry deposits: an experimental study of copper and gold partitioning at 850°C, 100 MPa in a haplogranitic melt – pyrrhotite – intermediate solid solution – gold metal assemblage, at gas saturation. *Lithos*, **46**, 573-589 (1999).
2. Bodnar, R. J., Burnham, C. W. and Sterner, S. M. Synthetic fluid inclusions in natural quartz. III. Determination of phase equilibrium properties in the system H₂O-NaCl to 1000°C and 1500 bars. *Geochim. Cosmochim. Acta* **49**, 1861-1873 (1985).
3. Bodnar, R. J. and Vityk, M. O. Interpretation of microthermometric data for H₂O NaCl fluid inclusions. in *Fluid Inclusions in Minerals, Methods and Applications*, (eds. De Vivo, B. and Frezzotti, M. L.) 117-130 (Virginia Polytechnic Institute, VA, 1994).
4. Chou, I. M. Oxygen buffer and hydrogen sensor techniques at elevated pressures and temperatures. in *Hydrothermal Experimental Techniques*, (eds. Ulmer G. C. & Barnes, H. L.) 61-69 (Wiley, New York, 1987).
5. Clemente, B., Scaillet, B. & Pichavant, M. The solubility of sulphur in hydrous rhyolitic melts. *J. Petrol.*, **45**, 2171-2196 (2004).
6. Morgan, G. B. & London, D. Optimizing the electron microprobe analysis of hydrous alkali aluminosilicate glasses. *American Mineralogist*, **81**, 1176-1185 (1996).
7. Acosta-Vigil, A., London, D., Morgan, G. B. & Dewers, T. A. Solubility of excess alumina in hydrous granitic melts in equilibrium with peraluminous minerals at 700-800°C and 200 MPa, and applications of the aluminum saturation index. *Contrib. Mineral. Petr.* **146**, 100-119 (2003).
8. Günther, D., Frischknecht, R., Heinrich, C. A. & Kahlert, H. J. Capabilities of an Argon fluoride 193 nm Excimer laser ablation inductively coupled plasma mass spectrometry microanalysis of geological materials, *J. Anal. Atomic Spec.* **12**, 939-944 (1997).
9. Günther, D., Audétat, A., Frischknecht, A. & Heinrich, C. A. Quantitative analysis of major, minor, and trace elements in fluid inclusions using laser ablation-inductively coupled plasma mass spectrometry. *J. Anal. Atom. Spec.* **13**, 263-270 (1998).
10. Heinrich, C. A. *et al.* Quantitative multi-element analysis of minerals, fluid and melt inclusions by Laser-Ablation Inductively-Coupled-Plasma Mass Spectrometry, *Geochim. Cosmochim. Acta* **67**, 3473-3497 (2003).
11. Pettke, T., Halter, W. E., Webster, J. D., Aigner-Torres, M. & Heinrich, C. A. Accurate quantification of melt inclusion chemistry by LA-ICP-MS: A comparison with EMP and SIMS and advantages and possible limitations of these methods. *Lithos*, **78**, 333-361 (2004).
12. Simon, A. C., Pettke, T., Candela, P. A., Piccoli, P. M. & Heinrich, C. A. Magnetite solubility and iron transport in magmatic-hydrothermal environments. *Geochim. Cosmochim. Acta* **68**, 4905-4914 (2004).
13. Simon A. C. *et al.* Gold partitioning in melt-vapor-brine systems. *Geochim. Cosmochim. Acta* **69**, 3321-3335 (2005).

Table 1. Probe conditions and analysis order of the four wavelength dispersive (WDS) X-ray spectrometers from the JEOL electron probe microanalyzer JXA-8900 (EPMA).

20 kV, 10 nA, 2 μm				
	1	2	3	4
MAJORS	TAP	PETH	LIF	TAP
	As	S	Fe	As
	Si	Ca		
Run Time (min)	2	2	1	1
20 kV, 100 nA, 2 μm				
	1	2	3	4
TRACE	TAP	PETH	LIF	TAP
	Zn	Hg	Ti	Zn
	Se	Ag	Co	Se
	Si	Te	Ni	
		Sb	Cu	
		Mo	Au	
		Sn	Tl	
		W	Bi	
		Pb		
Run Time (min)	3	9	21	2

Table 2. The suite of elements used to analyze pyrites in at the Turquoise Ridge deposit. The X-ray line, spectrometer, peak data, and calculated 3-sigma minimum detection limit (MDL) in ppm and wt% are listed for each element. All elements are quantified by using a 30 second counting interval on the peak and 15 second counting intervals on both the high and low background positions.

Element	X-ray	Spectrometer	Crystal	Peak (mm)	Back[H+] (mm)	Back[L-] (mm)	Peak (sec)	Back (sec)	MDL (ppm)	MDL (wt%)	MDL (cps)	Standard
Si	K α	SP1	TAP	77.357	2.25	2.25	30	15	49	0.0049		Mac-Wollastonite
S	K α	SP2	PETH	172.062	5.00	5.00	30	15	1,493	0.1493		Mac-FeS ₂
Ca	K α	SP2	PETH	107.585	2.50	3.00	30	15	465	0.0465		Mac-Wollastonite
Fe	K α	SP3	LIF	134.677	4.00	2.00	30	15	558	0.0558		Mac-FeS ₂
As	L α	SP1 & SP4	TAP	105.134	5.00	5.00	30	15	310	0.0310		Mac-Arsenic
Ti	K α	SP3	LIF	191.200	1.50	1.50	30	15	197	0.0197	9.4	SMH-Ilmenite
Co	K α	SP3	LIF	124.427	5.00	5.00	30	15	32	0.0032	8.6	GLR-Co
Ni	K α	SP3	LIF	115.270	4.50	4.50	30	15	163	0.0163	9.4	GLR-Ni
Cu	K α	SP3	LIF	107.120	2.80	2.80	30	15	186	0.0186	10.5	Mac-Chalcopyrite
Zn	L α	SP1 & SP4	TAP	133.214	5.00	5.00	30	15	176	0.0176	5.5	Mac-ZnS
Se	L α	SP1 & SP4	TAP	97.664	2.75	5.00	30	15	89	0.0089	7.5	CM1-Se
Mo	L β	SP2	PETH	165.800	1.00	1.25	30	15	282	0.0282	8	GLR-Mo
Ag	L β	SP2	PETH	133.257	2.00	2.00	30	15	97	0.0097	13.1	CM1-Ag
Sn	L β	SP2	PETH	115.281	1.50	1.50	30	15	145	0.0145	9.4	CM1-Sn
Sb	L β	SP2	PETH	110.153	4.00	4.00	30	15	111	0.0111	19	CM1-Sb
Te	L β	SP2	PETH	105.298	3.75	3.75	30	15	130	0.0130	20.2	CM2-PbTe
W	M α	SP2	PETH	223.597	3.00	3.00	30	15	375	0.0375	3.1	CM1-W
Au	L α	SP3	LIF	88.760	4.00	4.00	270	135	91	0.0091	4.5	GLR-Au
Hg	M α	SP2	PETH	180.774	2.40	2.40	120	60	97	0.0097	3.9	CM2-HgS
Tl	L α	SP3	LIF	84.309	1.20	0.98	120	60	426	0.0426	6.7	CM2-TlBr
Pb	M α	SP2	PETH	169.217	5.50	3.00	30	15	387	0.0387	4.1	Mac-PbS
Bi	L α	SP3	LIF	79.340	5.00	5.00	120	60	373	0.0373	9.9	CM1-Bi

Table 3. Representative analyses from the HGB, 148 and BBT ore zones in the Turquoise Ridge deposit.

Element	MDL wt. %	HGB Zone TU924 501 Grade 7.613 opt Au		148 Zone TU688 553 Grade 5.469 opt Au		BBT Zone TU929 761 Grade 0.061 opt Au	
		Core (wt.%)	Rim (wt.%)	Core (wt.%)	Rim (wt.%)	Core (wt.%)	Rim (wt.%)
Fe	0.038	45.862	38.416	46.159	37.706	46.354	39.465
S	0.020	53.763	46.653	53.52	42.539	53.998	48.981
As	0.040	0.843	11.678	1.043	15.633	0	8.253
Au	0.009	0	0.323	0	0.271	0	0.111
Hg	0.010	0	0.639	0	0.558	0	0.215
Tl	0.044	0.028	0.854	0	0	0	0.243
Sb	0.011	0	0.131	0.014	0.406	0	0.058
Cu	0.021	0.002	0.099	0.008	0.292	0.028	0.405
Te	0.013	0	0.151	0	0.477	0	0.044
Ag	0.010	0.01	0.001	0	0.006	0	0.005
Pb	0.070	0.043	0	0.05	0	0	0
Zn	0.018	0	0.005	0	0.006	0	0
Mo	0.029	0	0	0	0	0	0
Sn	0.028	0.001	0.005	0	0.001	0	0
W	0.078	0.006	0.026	0	0	0	0.003
Co	0.003	0.061	0.054	0.052	0.045	0.073	0.064
Ni	0.016	0.016	0	0.009	0.006	0.001	0
Ti	0.020	0.213	0.002	0	0.002	0	0
Se	0.009	0	0.013	0.011	0.023	0.014	0
Bi	0.073	0.047	0	0	0	0	0
Ca	0.014	0	0	0	0	0	0.08
Si	0.005	0.028	0.077	0.046	0.36	0.029	0.264
Total		100.923	99.127	100.912	98.331	100.497	98.191

MDL – mean detection limit

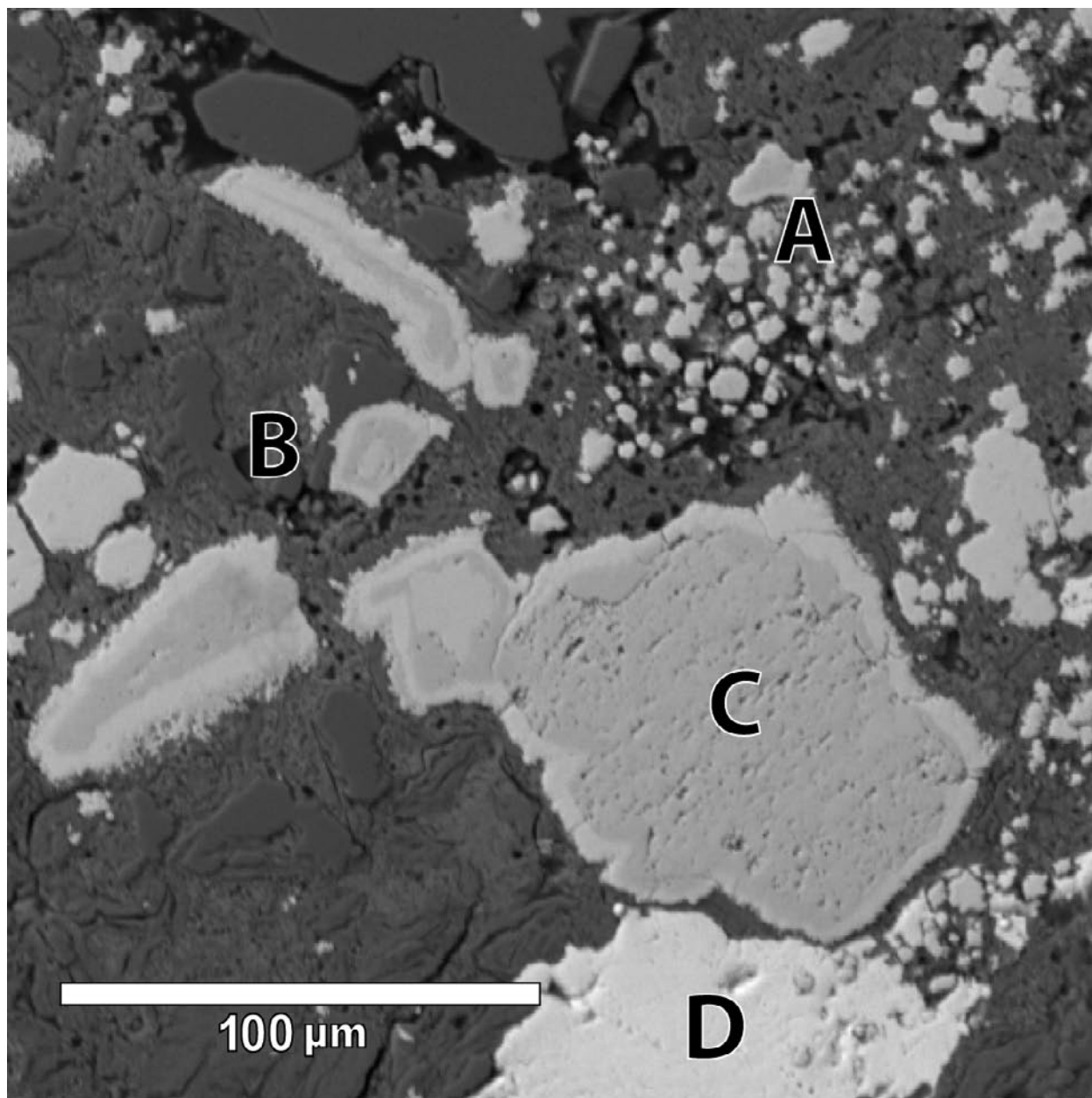


Figure 1. Back-scattered electron image showing typical ore-stage pyrites found at Turquoise Ridge. A. Spheroidal fuzzy pyrites that have trace element concentrations ranging from 2000-3000 ppm Au, 2500-3500 ppm Cu, 1000-1600 ppm Te, 500-1600 ppm Sb, 3000-7000 ppm Hg, 5000-10,000 ppm Tl, and >10 wt% As, as determined by EPMA. B. Strongly resorbed core-rim pyrites with multiple ore stage rims. Trace element concentrations range from 10-2400 ppm Au, 50-3300 ppm Cu, 230-1800 ppm Te, 90-750 ppm Sb, 45-7500 ppm Hg, 18-11,000 ppm Tl, and 0.3-12.0 wt% As. C. Corroded and resorbed pyrite core with later multiple stage rims. D. Late realgar with spheroidal fuzzy pyrites (right of D).